

Infrared Variability of the Gliese 569B System

Matthew A. Kenworthy¹

Leiden Observatory, Leiden University, P.O. Box 9513, 2300 RA Leiden, The Netherlands

and

Louis J. Scuderi¹

*Institute for Astronomy, University of Hawaii, 2680 Woodlawn Drive, Honolulu, HI
96822-1839, USA*

kenworthy@strw.leidenuniv.nl

ABSTRACT

Gliese 569B is a multiple brown dwarf system whose exact nature has been the subject of several investigations over the past few years. Interpretation has partially relied on infra-red photometry and spectroscopy of the resolved components of the system. We present seeing limited K_s photometry over four nights, searching for variability in this young low mass substellar system. Our photometry is consistent with other reported photometry, and we report the tentative detection of several periodic signals consistent with rotational modulation due to spots on their surfaces. The five significant periods range from 2.90 hours to 12.8 hours with peak to peak variabilities from 28 mmag to 62 mmag in the K_s band.

If both components are rotating with the shortest periods, then their rotation axes are not parallel with each other, and the rotation axis of the Bb component is not perpendicular to the Ba-Bb orbital plane. If Bb has one of the longer rotational periods, then the Bb rotation axis is consistent with being parallel to the orbital axis of the Ba-Bb system.

¹Steward Observatory, 933 North Cherry Avenue, Tucson, AZ 85721

1. Introduction

Gliese 569B was first discovered and identified as a comoving companion to nearby low mass star Gliese 569 ($d = 9.8$ pc, SpT=dM2) by [Forrest et al. \(1988\)](#), as part of a survey of nearby stars looking for brown dwarf candidates ([Skrutskie et al. 1989](#)). They concluded that the unusual red colors of this object suggested either a late-type M dwarf, a young brown dwarf still in the process of contracting, or an unresolved binary system. In the twenty years following the initial discovery, the true nature of this object has been difficult to determine due to the evolving state of low mass stellar models and the geometry of the system.

Visible band spectroscopic analysis of the B component ([Henry & Kirkpatrick 1990](#)) determined that it was similar to several late M-dwarfs and known brown dwarfs, eventually assigning it a spectral type of M 8.5. This model seemed to fit the data relatively well, as it was bluer than a known, similar age brown dwarf, but redder than a known late M star. With the advent of adaptive optics, GL 569B was resolved into two separate components, GL 569Ba and GL 569Bb ([Martín et al. 2000](#)). This paper was also able to constrain the age of the system to between 0.21 Gyr and 1.0 Gyr, and deduced that the total mass of the system to be $0.09 - 0.15M_{\odot}$ because of the observed lithium depletion and IR excess. They also estimated the orbital period to be on the order of ~ 3 years.

Following the discovery that the GL 569B component is (at least) a binary system, several papers examined the infrared colors of the system in J, H, and K. After an initial suggestion by [Martín et al. \(2000\)](#), it was claimed in [Kenworthy et al. \(2001\)](#) that the brighter component of the B system (GL 569Ba) is itself a double with masses roughly equivalent to the mass of the Bb component. This was based on the observations that (i) a blended two component system did not fit the data nearly as well as the original single M8.5 component, (ii) that the infrared colors were more consistent with a triple system, and (iii) both H and K band photometry showed a magnitude difference of 0.7 mag between the two components on two separate telescopes at two different epochs.

[Lane et al. \(2001\)](#) determined the mass function of the resolved components with a complete orbital solution and a revised age range of 200-500 Myr, assigning individual masses using relative colors. However, this paper found no evidence supporting the claim that the system was a triple, instead arguing for a double system with one component twice as massive as the other. This was based on their observed colors and astrometric data. [Zapatero Osorio et al. \(2004\)](#) then confirmed that the Bb component is the first genuine brown dwarf known without theoretical assumptions and calculated dynamical masses of the system. However, this group also found inconsistencies in models, noting that the observed surface gravity of each component was smaller than predicted by otherwise consistent evolutionary models. The conclusion reached by this paper, however, was that the 569B

system was a binary.

The relatively short period of the B system ($P \sim 2.4yr$), combined with the presence of a bright natural guide star suitable for adaptive optics assisted observations, has made this a well studied system (Lane et al. 2001; Zapatero Osorio et al. 2004; Martín et al. 2006; Simon et al. 2006; Dupuy et al. 2010; Konopacky et al. 2010; Femenía et al. 2011) Most recently, dynamical orbits for both Gliese 569B about the primary component A have been reported (Femenía et al. 2011) and more accurate orbital determinations of Bb about Ba have been presented in (Konopacky et al. 2010; Dupuy et al. 2010).

Simon et al. (2006) set out to measure the dynamical masses of Gliese 569B using the orbital motion of the 569B system about the A component. However, with an earlier age of 100 Myr and high resolution spectroscopy of the individual components, they concluded that Gliese 569B was a hierarchical triple brown dwarf system, with all three components having roughly equal masses of $0.04M_{\odot}$, which has been contested in subsequent literature of this object. Other researchers have determined masses for the 569B system assuming a two component model, summarised in Table 1.

One possible cause of this seeming discrepancy is that a component in the brown dwarf system Gliese 569B itself may be variable, and an indication of this is seen in K_s photometry in Kenworthy et al. (2001) and Lane et al. (2001). The purpose of this study is to determine if the system shows short term infra-red variability significant enough to explain the differing relative photometry of $\Delta K_s = 0.71 \pm 0.11$ in Kenworthy et al. (2001) and $\Delta K_s = 0.41 \pm 0.03$ seen by Lane et al. (2001), and to additionally look for signs of rotational modulation from the individual components.

Since Gliese 569B is one of the nearest young multiple brown dwarf systems, understanding its composition and activity is important in understanding the formation and evolution of low mass stellar systems. We describe the observations taken, their reduction and photometry in Section 2. The analysis of the photometry are presented in Section 3, the analysis of this data in Section 4 with our conclusions in 5.

2. Observations

Observations were carried out over 2003 April 20-24 UT using the 1.54m Kuiper Telescope on Mt. Bigelow. Data on 2003 April 22 UT was lost due to weather, with observations made on the remaining four nights. The camera (Williams et al. 1993) uses a NICMOS3 256x256 $40\mu m$ pixel InSb array, formed from four separate quadrants of 128x128 pixels. Each quadrant has a separate set of readout electronics, and the quadrant we use has a

gain of $15.3 e^-/\text{ADU}$ and a read noise of 73 electrons. The camera is set at the $0.33''/\text{pixel}$ scale for all nights resulting in a field of view of 42 by 42 arcseconds. All images are taken using the K_s filter, which has half-power points at $1.99\mu\text{m}$ and $2.32\mu\text{m}$. The photometric calibration we use relies on observations alternating between the target system and a nearby reference star. The field of view of the camera is not large enough to capture both the target object and the standard star in the same frame, and so each night of observations consists of two interleaved series of data. Observations were taken throughout the entire night, but the time resolution of the data are slightly reduced because of the time required to repoint the telescope between images.

All night followed both Gliese 569 and the reference star through transit at an airmass of 1.04, following the objects until sunrise at a typical airmass of 1.4 to 1.54. All data were fit with a circular Gaussian function to determine the seeing on each of the four nights - they were 1.20, 1.38, 1.27 and 0.94 arcseconds respectively, with a typical variation in measured seeing of 0.18 arcseconds. The mean seeing over all four nights was 1.20 arcseconds.

Several candidate standard stars were selected from the 2MASS all sky catalog to be of a similar magnitude to the target system of Gl 569B. This list was further refined for proximity to the science target, catalog quality of the photometry and lack of variability as indicated in the 2MASS catalog. The reference star we use is 2MASS 14545403+1602042 $J = 9.706 \pm 0.020$; $H = 9.249 \pm 0.019$; $K = 9.144 \pm 0.020$ (Cutri et al. 2003). The spectral type of the standard star is estimated to be K0-K2 from the visible and near infrared colors, and estimated to be 120pc distant. Each data frame consists of 30 coadded exposures of 2 seconds duration, resulting in a total on sky integration of 60 seconds per data frame. The sky background flux is approximately 30 counts at 1.06 airmasses up to 65 counts at 1.50 airmasses. Gliese 569B has a typical peak value of 250 counts above the sky background level, within the linear response of the detector. All four nights were clear with no significant cloud cover. Data reduction is carried out with a combination of IRAF and PDL scripts.

Dark frames and flat fields were taken with the same exposure time and readout mode for each night. Twilight flats were taken on the nights of 23 and 24 April. An investigation of the dark frames show a drift in count levels over a course of integrations, with the drift approximated by a gradient from 3 to 8 counts across each separate quadrant of the array between two successive integrations. As a consequence of this effect, the dark frame and sky background is removed by beam switching. Each science frame has the closest standard star frame in time subtracted from it, resulting in a cosmetically clean image with a small DC component from the change in sky background between frames (see Figure 1). The residual sky flux is removed by computing the median value of a box containing only sky background.

Flat field images were constructed using images of the sky with the telescope tracking

switched off. Dark frames, taken just before the flat field images, are subtracted off the flat field frames. These dark subtracted sky images are then combined together with *IMCOMBINE*, scaling by the mean sky flux and with sigma clipping to reject any faint star trails that remain in the frame. The flat field frames are then normalised by the mean flux within the quadrant containing the stellar images. These flat fields are divided into the science observations. To examine the repeatability of the flat fields between nights, we produced flat field frames for the nights of 23 and 24 April and divided one into the other. The resultant image shows a flat image dominated by Gaussian noise with no significant spatial structure. The flat fields themselves show low spatial structure gradients in the science region of the images, with no significant flaky or dead pixels in the region of interest.

3. Photometry and Analysis

The slew of the telescope takes approximately ten seconds from target to reference, and oscillations in the telescope structure take several seconds to die down to subarcsecond amplitudes. To account for this, a parameter in the camera control software introduces a fixed delay before starting the next exposure. In order to maximise our observing efficiency, we reduced this delay parameter to 6 seconds. Subsequent examination of the images showed that in several cases, the oscillations had not completely died down, leading to an elongation of the stellar image in the direction of the telescope slew. The elongation of the science and reference star images is not consistent, and so we could not use PSF fitting for data analysis. Furthermore, the core of the Gliese 569A component was deliberately saturated on the detector, to enable photometry of the fainter B system. As a consequence of these two effects, we use aperture photometry for the data reduction.

Each of the four nights had good natural seeing, allowing for aperture photometry. We use a custom PDL routine to identify the G1569B component and reference star in all the images. The IRAF *phot* routine is run on all the data with three extraction apertures, 3.0, 4.0 and 5.0 pixels in radius. Because the telescope had to be repointed each time an image was taken, the standard star images and the target star images are taken in an alternating sequence. We linearly interpolate the instrumental magnitude of adjacent standard star exposures to the time of the target star observations. This interpolated standard star magnitude is then subtracted off the G1569B magnitude, and this process is repeated for all three aperture sizes. The estimated photometric error is typically 0.020 magnitudes for the G1569B frames. This error is estimated from the noise contributions of the measured sky background (which includes contributions from the beam switching process, the read noise and dark current of the detector) and the flux of G1 569B. This process is shown in Figure

2.

Each photometric measurement of GL 569B is calculated as $M(K_s) = dm + m(K_s) - DM$, where dm is the measured magnitude difference, $m(K_s)$ the K-band 2MASS magnitude of the standard star, and DM is the correction from apparent to absolute magnitude for Gliese 569B ($\pi = 0.10359 \pm 0.00172$; van Leeuwen 2007). The Kuiper K_s filter is similar in bandwidth to the MKO K_s filter. The conversions from the 2MASS filter to the MKO K band filter is on the order of -0.01 magnitudes (Dupuy et al. 2010). We do not apply any corrections for the airmass, and we do not apply any color transformations from the Kuiper telescope filter to the 2MASS K filter system, as any systematic corrections are on the order of 0.015 for our observations.

Since the PSF of the standard star and the science target vary due to the telescope slew, we compared the final differential photometry for all three aperture sizes. The four nights of data are shown in Figure 3, where for each data point, the central filled circle represents the differential photometry for the $r = 4$ pixel ($r = 1.1$ FWHM) aperture, and the upper and lower ends of the vertical bar represent the $r = 3$ pixel ($r = 0.8$ FWHM) and $r = 5$ pixel ($r = 1.6$ FWHM) aperture extractions respectively. Ideally, the differential photometry of all three aperture extractions should be consistent with each other, within the photometric errors of the individual extractions, which are on the scale of the diameter of the circles used in Figure 3. For a majority of the points, the three different aperture extractions agree with each other to within photometric errors, but there are on order of 31 points over the four nights which report a significant spread in extracted photometry. For most of these cases they are related to manual focus changes in the camera optics, telescope vibrations, wind shake, and changes in the native seeing over several minutes. They can also be attributed to the scattered flux from Gliese 569A which is 5 arcseconds away. These points are rejected from further analysis.

Using the *psfextract* routine to fit a two-dimensional Gaussian to the stellar PSFs, we looked for correlations of photometric variability with the measured FWHM and ellipticity. In several cases we identified anomalous photometry with poor seeing in either the standard or target stars. We rejected these points from further consideration and mark these as grayed circles and lines. Our criterion for rejecting a data point is one where there is more than 0.1 magnitude spread in differential photometry between the largest and smallest apertures used in the extraction.

After the rejection of frames with poor photometry, we are left with an irregularly sampled set of data covering three timescales - the 24 hour period of the observations, a seven hour period of the visibility of the target from the observatory, and a several minute period due to the alternating observations between reference star and GJ 569B. We look for

sinusoidal periodicities in this irregularly sampled data set by performing a Lomb-Scargle (LS) periodogram analysis on the photometric data, as outlined in Press et al. (1992) Section 13.8. We construct false alarm probabilities (FAP) for the LS analysis using the method described in the previous reference.

4. Discussion

4.1. Short-term Variability from Rotational Modulation

Both Ba and Bb show broadened absorption lines in infrared spectra in comparison to theoretical models (Zapatero Osorio et al. 2004). In a spectral analysis, Zapatero Osorio et al. (2004) suggest that this broadening is due to rotation of the components, and they derive projected rotational velocities of $v_{rot} \sin i = 37 \pm 15 \text{ km.s}^{-1}$ and $v_{rot} \sin i = 30 \pm 15 \text{ km.s}^{-1}$ for Ba and Bb respectively, where the uncertainty of the measurements is associated with a poor knowledge of the molecular opacities used in the model spectra used as templates. To overcome this, Simon et al. (2006) use observations of Gliese 644C as a template for their modeling, and they determine projected rotational velocities of $v_{rot} \sin i = 25 \pm 5 \text{ km.s}^{-1}$ and $v_{rot} \sin i = 10 \pm 2 \text{ km.s}^{-1}$ for Ba and Bb (the errors on the measurements are given by the velocity intervals of the rotationally broadened templates - Simon, priv. commun.), where the analysis was carried out at H band in the spectral orders 48 and 49 of NIRSPEC. A more recent analysis by Konopacky et al. (2012) using K band spectra with NIRSPEC and synthetically generated spectra using the PHOENIX atmosphere models yields projected rotational velocities of $v_{rot} \sin i = 19 \pm 2 \text{ km.s}^{-1}$ and $v_{rot} \sin i = 6 \pm 3 \text{ km.s}^{-1}$ for Ba and Bb respectively. The Konopacky et al. (2012) measurements agree with the Simon et al. (2006) measurements at the 1σ level, but show a systematically smaller projected rotation velocity. In the subsequent analysis, we use the combined weighted measurements from both Konopacky et al. (2012) and Simon et al. (2006), where $v_{rot} \sin i = 19.8 \pm 1.9 \text{ km.s}^{-1}$ and $v_{rot} \sin i = 8.8 \pm 1.7 \text{ km.s}^{-1}$ for Ba and Bb.

For a range of plausible models of stellar radii, limited by uncertainties in the age of the stars, Zapatero Osorio et al. (2004) pointed out that the rotational periods of Ba and Bb would be on the order of $3 \sin i$ and $5 \sin i$ hours respectively. More specifically, given a radius of $0.11 R_{\odot}$, the rotational periods (in hours) are $6.7 \sin i_{Ba}$ and $15.2 \sin i_{Bb}$ where i is the angle of inclination between the rotation axis of the object and our line of sight. Any rotational modulation should be present at periods shorter than these periods, and these candidate rotational periods are indicated with vertical lines in Figure 4. The Lomb-Scargle periodogram in Figure 4 shows two equal power peaks with false alarm probabilities (FAP) of $<10\%$ at 3.320 ± 0.035 hours and 2.905 ± 0.030 hours (where we have determined the errors

on the periods as the full width at half power in the periodogram) indicated with tick marks in the figure. These are candidate periods for both Ba and Bb. Although the individual peaks have relatively large FAPs associated with them, these are the two most significant peaks over plausible rotational periods for both Ba and Bb with nearly identical amounts of power present. We looked for these periods in subsets of the complete time series, but it requires at least a three day coverage to provide the temporal resolution in the Lomb-Scargle periodogram for these two periods. We see these two periods at a lower significance when we remove the data from either the first day or the last day from our analysis.

Since Bb has a lower projected broadening velocity, a larger range of periods can be considered, as indicated in Figure 4 with significant periods at 7.5 ± 0.1 h, 11.0 ± 0.5 h and 12.8 ± 0.7 h. The errors on the period determination are noticeably broader as these periods cover a larger fraction of the total photometric time series measured.

Folded light curves for all five periodicities, along with the best sinusoidal curve fits are shown in Figure 5. All the light curves show departures from an exact sinusoidal variation. The peak to peak amplitude of these fluctuations are listed in Table 2. We determined the errors on the amplitudes of the fitted sinusoidal functions by increasing the amplitude of the fitted period and calculating the full χ^2 value. When this chi-squared value had increased by the mean value of the reduced chi-squared, we use the delta in fitted amplitude as an estimate for the error in the fit. For Ba, the most significant periods are the 3.320 and 2.905 hours, but because of the lower rotational broadening seen in Bb, there are additionally significant periods and amplitudes at 7.5, 11 and 12.8 hours for Bb only.

Variability on these time scales and at these amplitudes is seen in other late M/early L stars, such as BRI 0021-0214 (Martín et al. 2001) and young stars such as S Ori 45 (Zapatero Osorio et al. 2003). Indeed, variability is seen with peak to peak values of 30 to 60 mmag (Lane et al. 2007; Artigau et al. 2009) and in the K_s band, Enoch et al. (2003) see variability with an amplitude of 0.2 magnitudes for objects at the L/T transition. The longest period consistent with the hypothesis of stellar spot modulation shows a slightly higher χ_{red}^2 goodness of fit, and a significantly lower peak amplitude compared to the shorter period amplitudes. There is also power seen at longer periods which, if real, cannot be due to rotational modulation in Ba. We attribute these to slowly evolving dust cloud features (Martín et al. 2001; Bailer-Jones & Mundt 2001), but simultaneous observations at other wavelengths are required to test the origin of these variations.

We emphasise that we cannot uniquely determine what components are responsible for the periodic signals we are detecting from this seeing limited data set. We can, however, model what the derived inclinations would be for different combinations of periods with the Gliese 569 B components.

4.2. Derived Inclinations of the Rotational Axes of Gliese 569Ba and Bb

In order to see what the inclination angle of the rotational axes for Ba and Bb are, we solved the equation $\sin i = (v_{rot} \sin i).P/(2\pi R)$ for i , where P is the rotational period of the low mass component and R is the radius of the low mass component. To propagate the errors in the measurements of v_{rot} , $\sin i$, P and R , we run a Monte Carlo simulation of 100000 runs where values for each of the input parameters are drawn from normal distributions with sigmas equal to their respective quoted errors. The resultant distributions of the inclination angle are then constructed and normalised to the peak value.

4.2.1. Ba and Bb both have short rotational periods

We first consider the case where both Ba and Bb have rotational periods shorter than 6.5 hours. We are motivated to do this because the FAP of the two most significant periods are approximately equal in size. The resultant distributions of i for each component are shown in Figure 6. It is not known which rotational period belongs to Ba or Bb, so we perform one set of simulations with Ba having the longer of the two periods, and then we rerun the simulations with the two periods swapped between the two components. The resultant distributions in rotational axis inclination are shown as histograms in Figure 6. We quote the measurement and uncertainties in inclination angle as confidence limits at 15.9% and 84.1% completeness of the distributions (equivalent to 1σ limits in a Normal distribution) and these are represented as the dark grey boxes on top of each distribution. The dotted vertical line in all the plots represents the inclination of the perpendicular to the orbital plane of the Ba-Bb system ($i = 33.6^\circ$; Konopacky et al. 2010).

The radii of Ba and Bb are estimated in Konopacky et al. (2010) by fitting PHOENIX models to measured photometry. In the upper row of plots in Figure 6 we use these values and errors on the radii as input to our simulations, $R_{Ba} = 1.69 \pm 0.09R_{jup}$ and $R_{Bb} = 1.28 \pm 0.07R_{jup}$. The resultant distributions for i_{Ba} and i_{Bb} show that both Ba and Bb have their rotational axes tilted with respect to one another by approximately 10 degrees, regardless of which component has the faster rotation period. Furthermore, both rotational axes are significantly tilted with respect to the perpendicular of their mutual orbital plane, i.e. the spin-orbit inclination i_{rel} is non-zero.

To see how robust this result was, we perform a second set of simulations where we expand the radii of both components to cover a much wider range of possible radii (including the $0.11R_\odot$ radius used earlier) - $R_{Ba} = R_{Bb} = 1.0 \pm 0.3R_{jup}$ and the results form the lower pair of plots in Figure 6. In this case, both distributions of axial inclination are

broader (which is to be expected) and Ba’s rotation axis may be consistent with the orbital inclination. However, the relative tilt of the rotational axes with respect to each other remains significant.

4.2.2. *Bb has a longer rotational period*

We now consider if Bb has the longer rotational period at 7.5, 11 or 12.8 hours. We run a set of Monte Carlo simulations assuming the same radius for Bb as derived from the PHOENIX models in the previous section. The resultant inclination angle distributions are shown in Figure 7. For 11.0 and 12.8 hours, the inclination of Bb is consistent with a spin-orbit inclination of zero, although at a lower level of confidence than with the shorter periods in the previous section. At the shortest of the three periods, there is evidence that Bb may have a spin-orbit inclination of approximately ten degrees.

5. Conclusions

We draw three main conclusions from our data and analysis.

The data presented here cover four days of photometric monitoring, where there is no variability in the Gliese 569B system large enough to explain the difference in relative brightness at K_s between Ba and Bb seen in Kenworthy et al. (2001) and Lane et al. (2001). Our first conclusion is that there is an unaccounted systematic error in the data reductions of one or both groups. The photometry we present in this paper is consistent with other measurements in the literature (e.g. see Forrest et al. 1988; Martín et al. 2000; Kenworthy et al. 2001; Lane et al. 2001; Simon et al. 2006; Dupuy et al. 2010).

Analysis of the time series of data presented in this paper show variability in the Gliese 569B system above that expected for measurement noise alone. Our analysis shows the presence of five periodicities from 3.32 to 12.8 hours with a peak to peak amplitude of 0.04 to 0.06 magnitudes, consistent with variability seen in other young low mass star systems.

If we attribute the periodicity in the light curve to rotational modulation of starspots on Ba and Bb, we can draw two further conclusions. Assuming Ba is a single object and that one of the two shorter periods is from Ba, then the rotational axis of Ba is not parallel to the orbital axis of the Ba-Bb system for fitted PHOENIX models of the radius of Ba. If this result is confirmed independently, it will be interesting to determine whether this spin-orbit misalignment is primordial in nature or due to subsequent interactions from the third, more massive 569 A component. Currently few stellar examples exist, although misaligned disks in

triple systems have also been detected (Skemer et al. 2008). To determine the contribution of 569A, further astrometry is required. Currently the orbital period of A about B is estimated to be approximately 400 years, with a low ellipticity constraint (Femenía et al. 2011).

If the Ba and Bb components are responsible for the two shortest periods, then we can robustly say that the Ba and Bb rotational axes are not aligned with respect to each other. Alternatively, if Bb is responsible for one of the 7.5 or longer periods, then Bb’s rotation axis is aligned with the orbital axis of the Ba-Bb system. The conclusion that Ba’s rotational axis is inclined to the spin-orbit axis remains valid.

Future work should include a longer and more sensitive photometric observing campaign to confirm the rotational modulation. More long term monitoring will begin to investigate the shape of the modulated light curve and determine if we are seeing the effects of clouds in the atmospheres of this multiple brown dwarf system. Longer monitoring with an adaptive optic telescope will allow splitting of the components and confirmation of the separate rotational periods. Higher spectral resolution measurements in the individual 569B components will begin to constrain the theoretical models of these objects, assuming the spectral line broadening is due to stellar rotation.

Gliese 569B is a benchmark system whose proximity and bright components will lead to further investigations and act as an ongoing test for low mass stellar models.

REFERENCES

- Artigau, É., Bouchard, S., Doyon, R., & Lafrenière, D. 2009, *ApJ*, 701, 1534
- Bailer-Jones, C. A. L. & Mundt, R. 2001, *A&A*, 367, 218
- Cutri, R. M., Skrutskie, M. F., van Dyk, S., Beichman, C. A., Carpenter, J. M., Chester, T., Cambresy, L., Evans, T., Fowler, J., Gizis, J., Howard, E., Huchra, J., Jarrett, T., Kopan, E. L., Kirkpatrick, J. D., Light, R. M., Marsh, K. A., McCallon, H., Schneider, S., Stiening, R., Sykes, M., Weinberg, M., Wheaton, W. A., Wheelock, S., & Zacarias, N. 2003, *2MASS All Sky Catalog of point sources*.
- Dupuy, T. J., Liu, M. C., Bowler, B. P., Cushing, M. C., Helling, C., Witte, S., & Hauschildt, P. 2010, *ApJ*, 721, 1725
- Enoch, M. L., Brown, M. E., & Burgasser, A. J. 2003, *AJ*, 126, 1006

- Femenía, B., Rebolo, R., Pérez-Prieto, J. A., Hildebrandt, S. R., Labadie, L., Pérez-Garrido, A., Béjar, V. J. S., Díaz-Sánchez, A., Villó, I., Oscoz, A., López, R., Rodríguez, L. F., & Piqueras, J. 2011, *MNRAS*, 413, 1524
- Forrest, W. J., Shure, M., & Skrutskie, M. F. 1988, *ApJ*, 330, L119
- Henry, T. J. & Kirkpatrick, J. D. 1990, *ApJ*, 354, L29
- Kenworthy, M., Hofmann, K.-H., Close, L., Hinz, P., Mamajek, E., Schertl, D., Weigelt, G., Angel, R., Balega, Y. Y., Hinz, J., & Rieke, G. 2001, *ApJ*, 554, L67
- Konopacky, Q. M., Ghez, A. M., Barman, T. S., Rice, E. L., Bailey, J. I., White, R. J., McLean, I. S., & Duchêne, G. 2010, *ApJ*, 711, 1087
- Konopacky, Q. M., Ghez, A. M., Fabrycky, D. C., Macintosh, B. A., White, R. J., Barman, T. S., Rice, E. L., Hallinan, G., & Duchene, G. 2012, *ApJ*, in press
- Lane, B. F., Zapatero Osorio, M. R., Britton, M. C., Martín, E. L., & Kulkarni, S. R. 2001, *ApJ*, 560, 390
- Lane, C., Hallinan, G., Zavala, R. T., Butler, R. F., Boyle, R. P., Bourke, S., Antonova, A., Doyle, J. G., Vrba, F. J., & Golden, A. 2007, *ApJ*, 668, L163
- Martín, E. L., Brandner, W., Bouy, H., Basri, G., Davis, J., Deshpande, R., & Montgomery, M. M. 2006, *A&A*, 456, 253
- Martín, E. L., Koresko, C. D., Kulkarni, S. R., Lane, B. F., & Wizinowich, P. L. 2000, *ApJ*, 529, L37
- Martín, E. L., Zapatero Osorio, M. R., & Lehto, H. J. 2001, *ApJ*, 557, 822
- Press, W. H., Teukolsky, S. A., Vetterling, W. T., & Flannery, B. P. 1992, *Numerical recipes in C. The art of scientific computing*
- Simon, M., Bender, C., & Prato, L. 2006, *ApJ*, 644, 1183
- Skemer, A. J., Close, L. M., Hinz, P. M., Hoffmann, W. F., Kenworthy, M. A., & Miller, D. L. 2008, *ApJ*, 676, 1082
- Skrutskie, M. F., Forrest, W. J., & Shure, M. 1989, *AJ*, 98, 1409
- van Leeuwen, F., ed. 2007, *Astrophysics and Space Science Library*, Vol. 350, *Hipparcos, the New Reduction of the Raw Data*

- Williams, D. M., Thompson, C. L., Rieke, G. H., & Montgomery, E. F. 1993, in Presented at the Society of Photo-Optical Instrumentation Engineers (SPIE) Conference, Vol. 1946, Proc. SPIE Vol. 1946, p. 482-489, Infrared Detectors and Instrumentation, Albert M. Fowler; Ed., ed. A. M. Fowler, 482–489
- Zapatero Osorio, M. R., Caballero, J. A., Béjar, V. J. S., & Rebolo, R. 2003, A&A, 408, 663
- Zapatero Osorio, M. R., Lane, B. F., Pavlenko, Y., Martín, E. L., Britton, M., & Kulkarni, S. R. 2004, ApJ, 615, 958

Facilities: Kuiper 61 inch Telescope.

We thank the anonymous referee for many useful comments and suggestions which have improved this paper and for their patience with these revisions. We thank Marcia and George Rieke for their support of the 256² IRCAM that made these observations, and to Chad Engelbracht for many useful discussions on infra red arrays and the data processing required. MAK and LS were supported by grant NNG 06-GE26G from the NASA Terrestrial Planet Finder Foundation Science Program. This research used the SIMBAD database, operated at CDS, Strasbourg, France, and data products of 2MASS, which is a joint project of the University of Massachusetts and IPAC at the California Institute of Technology, funded by NASA and NSF, and NASA’s Astrophysical Data System.

Table 1. Masses determined for the Gliese 569B system as reported in the literature. Data from Table 7 in [Femenía et al. \(2011\)](#), where corrections for the revised parallax of the 569B system ([van Leeuwen 2007](#)) have been applied.

Paper	Gliese 569B mass (M_{\odot})	Ba (M_{\odot})	Bb (M_{\odot})
Zapatero Osorio et al. (2004)	0.119 ± 0.005	0.071 ± 0.011	0.054 ± 0.011
Simon et al. (2006)	0.119 ± 0.007	0.100 ± 0.011	—
Konopacky et al. (2010)	0.120 ± 0.007	0.073 ± 0.008	0.053 ± 0.006
Dupuy et al. (2010)	$0.140^{+0.009}_{-0.008}$	0.075 ± 0.004	0.065 ± 0.004
Femenía et al. (2011)	0.116 ± 0.007	0.081 ± 0.010	0.059 ± 0.007

Table 2. Periods and fitted sinusoidal amplitudes from the Gliese 569B light curve

Period (h)	Peak to Peak Amplitude (mmag)	χ_{red}^2
3.320 ± 0.035	48 ± 8	6.5
2.905 ± 0.030	42 ± 8	6.3
7.5 ± 0.1	52 ± 10	6.3
11.0 ± 0.5	68 ± 8	6.2
12.8 ± 0.7	28 ± 10	7.0

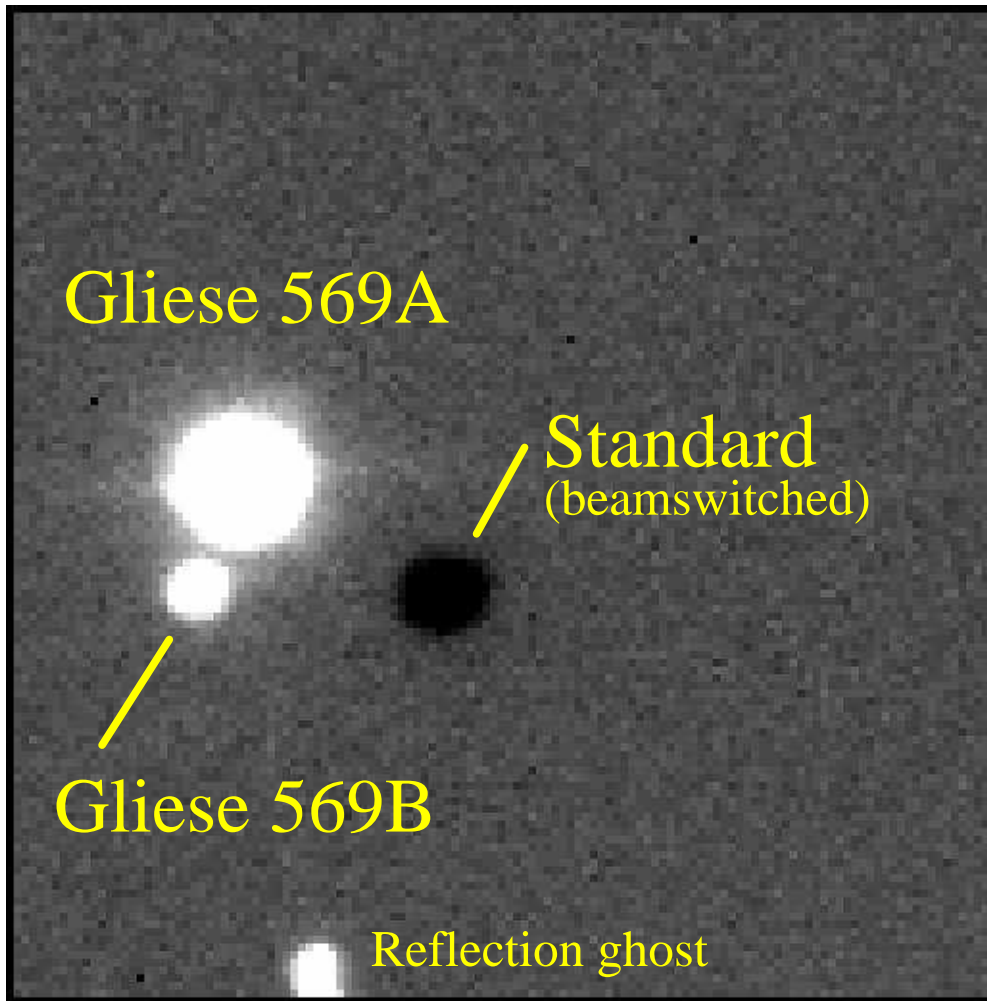


Fig. 1.— Beamswitched image from quadrant [129:256,1:128] of the camera array. The Gliese 569A star and 569B system are seen as positive flux sources, and the standard star is shown as the negative flux source. Displayed with a linear grayscale from -100 to +100 data counts.

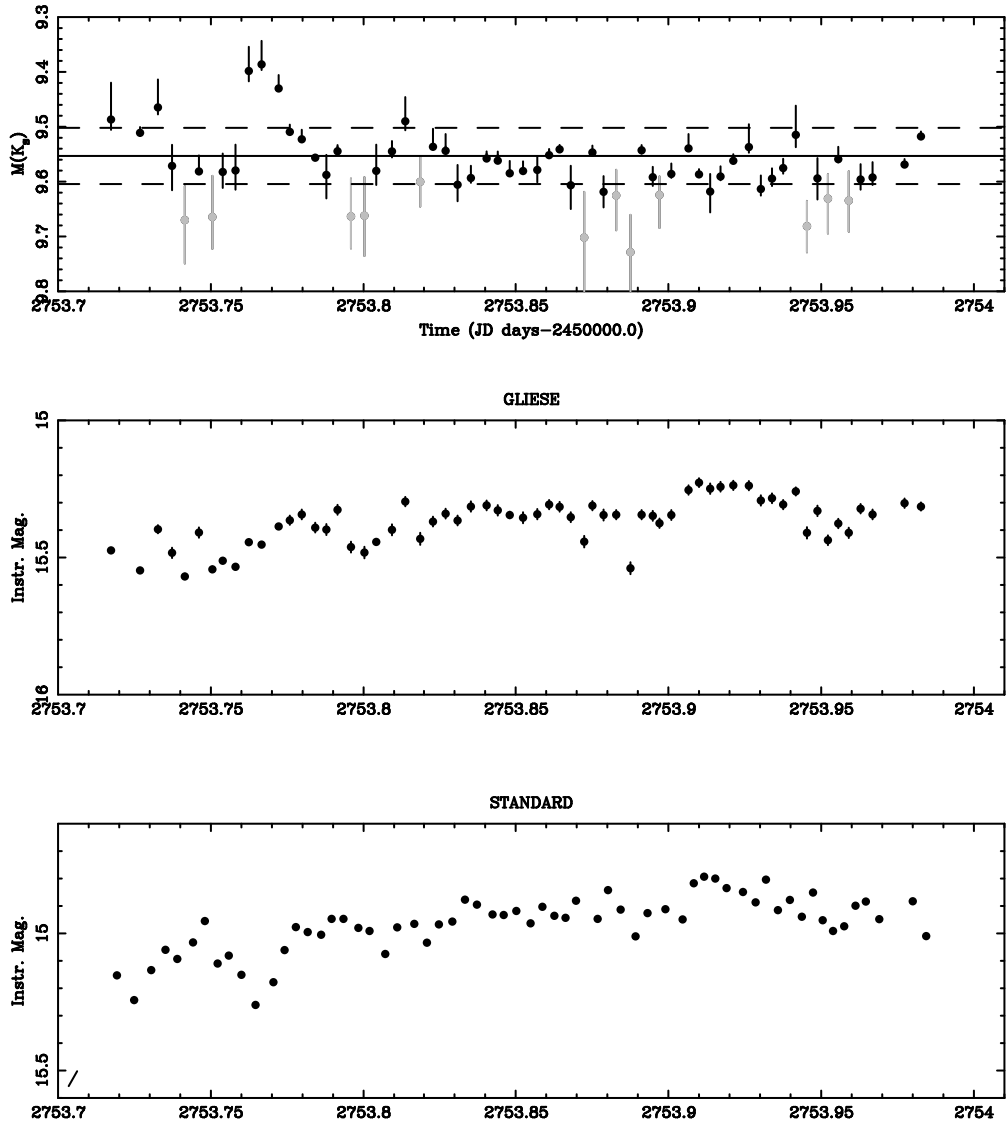


Fig. 2.— The reduced light curve for Gliese 569B on 23 April 2003 (top panel), with the uncalibrated photometry for Gliese 569B and the standard star shown below. Both lower plots show variations of 0.1 to 0.2 magnitudes, with a slight low order curve attributable to the airmass. The top curve shows the absolute K_s magnitude of the system. The black dots are photometry from $r = 4$ pixel apertures. The vertical bars on each point represent aperture photometry for $r = 3$ and $r = 5$ apertures. Points with significant variation in aperture photometry are rejected and are marked in light gray points. The horizontal line represents the mean value of the black points, and the dashed lines marking the r.m.s.

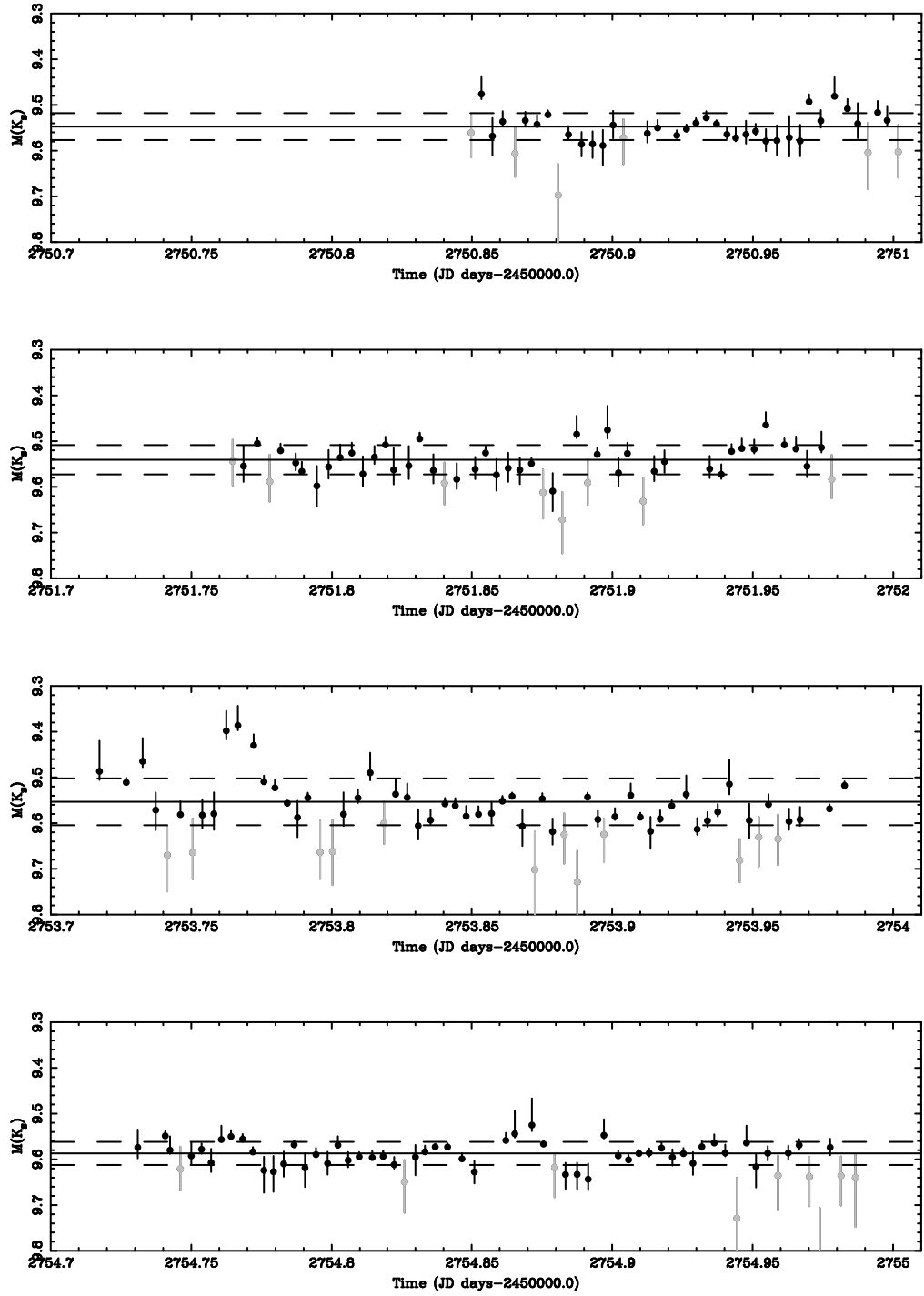


Fig. 3.— Photometry of Gliese 569B over the dates of 2003 April 20-24 UT. Symbols as in Figure 2

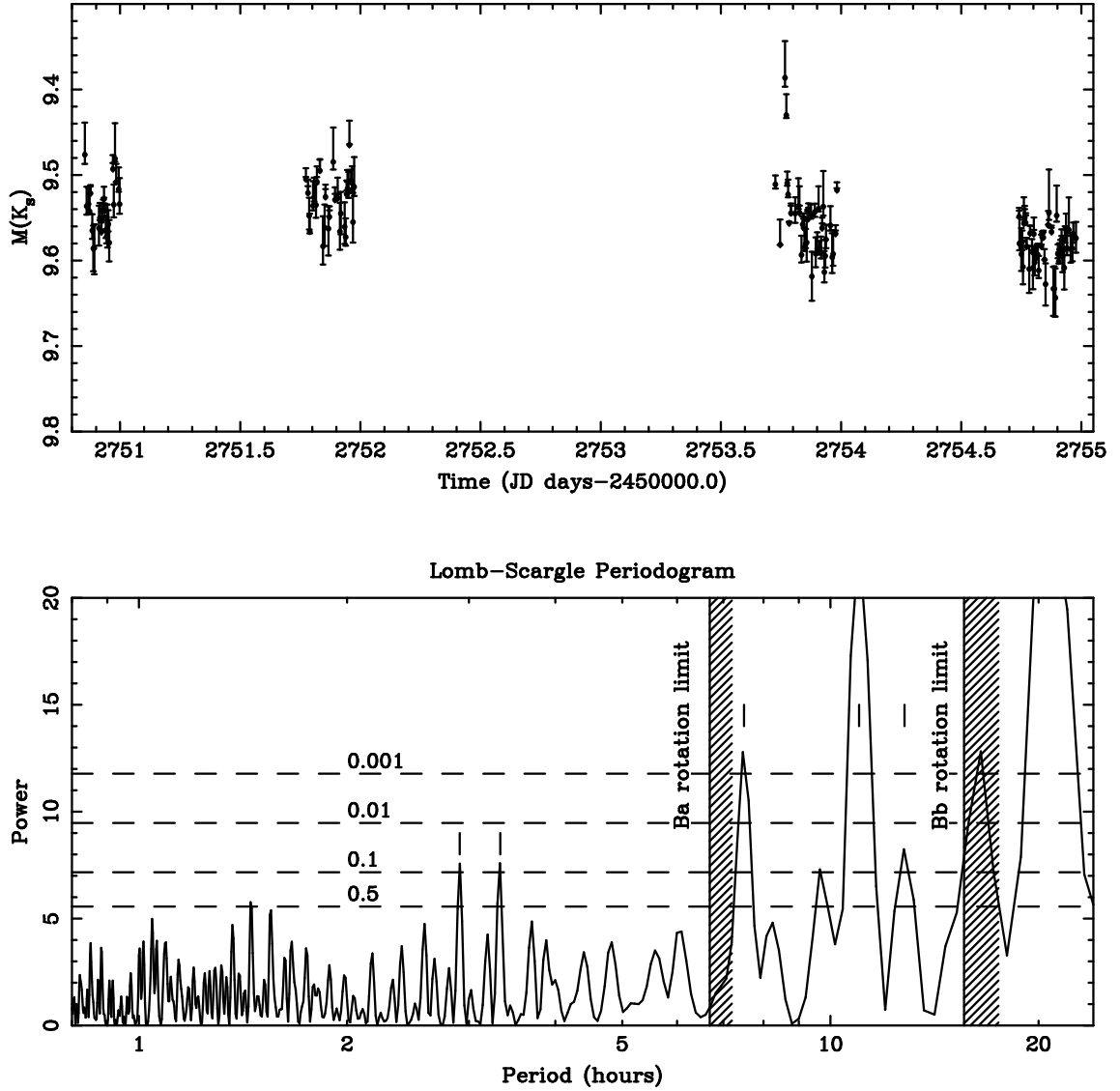


Fig. 4.— Time series photometry and Lomb Scargle periodogram of Gliese 569B. The upper panel shows the time series photometry, and the lower panel shows the Lomb Scargle periodogram for the data. The horizontal lines indicate different levels of False Alarm Probability for the detected power. The shaded regions indicate the longest allowed rotational periods given the projected velocities for Ba and Bb.

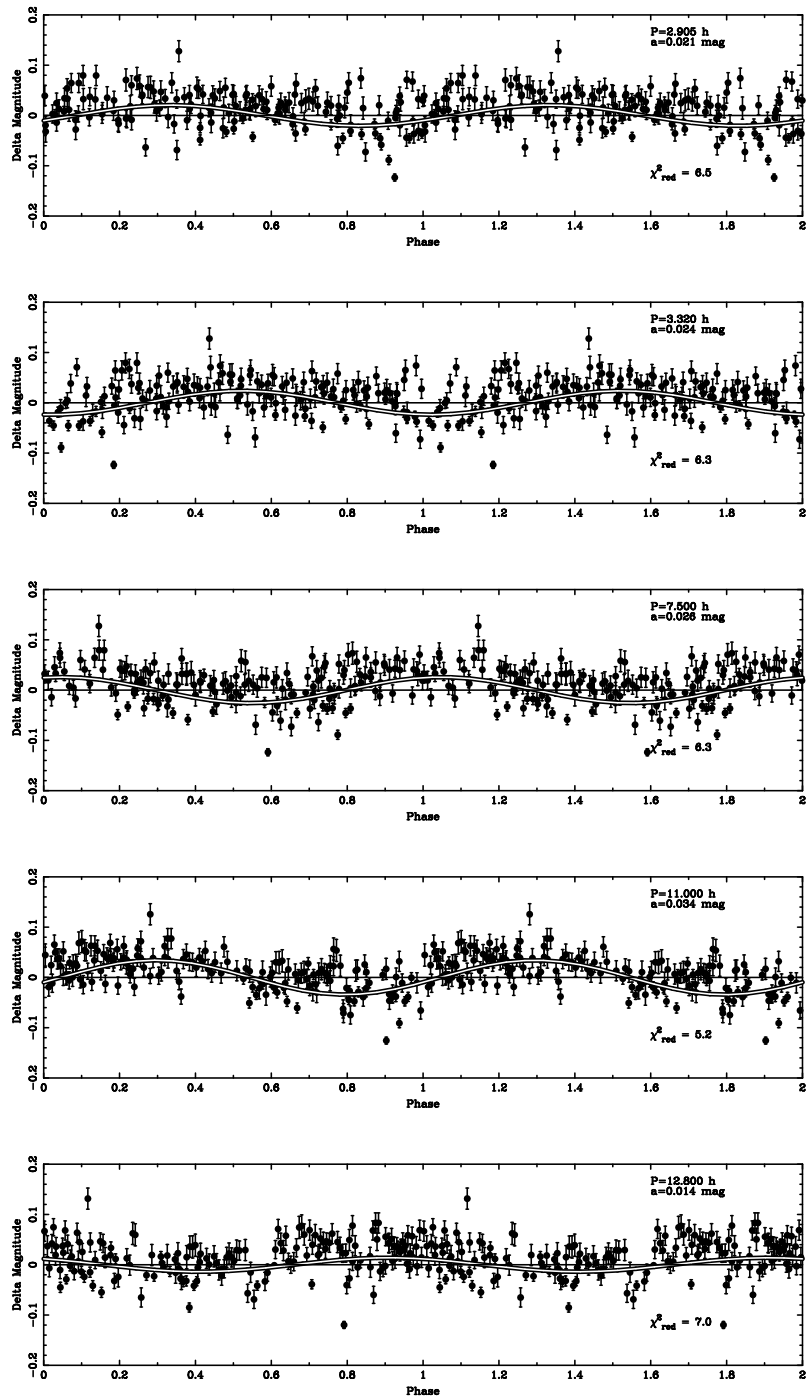


Fig. 5.— Folded light curves of the Gliese 569B photometry for the periods listed in Table 2. The phase coverage is extended over two periods for clarity. The best fit sinusoid is drawn over the folded light curve with the best fit amplitude indicated in the figure panels.

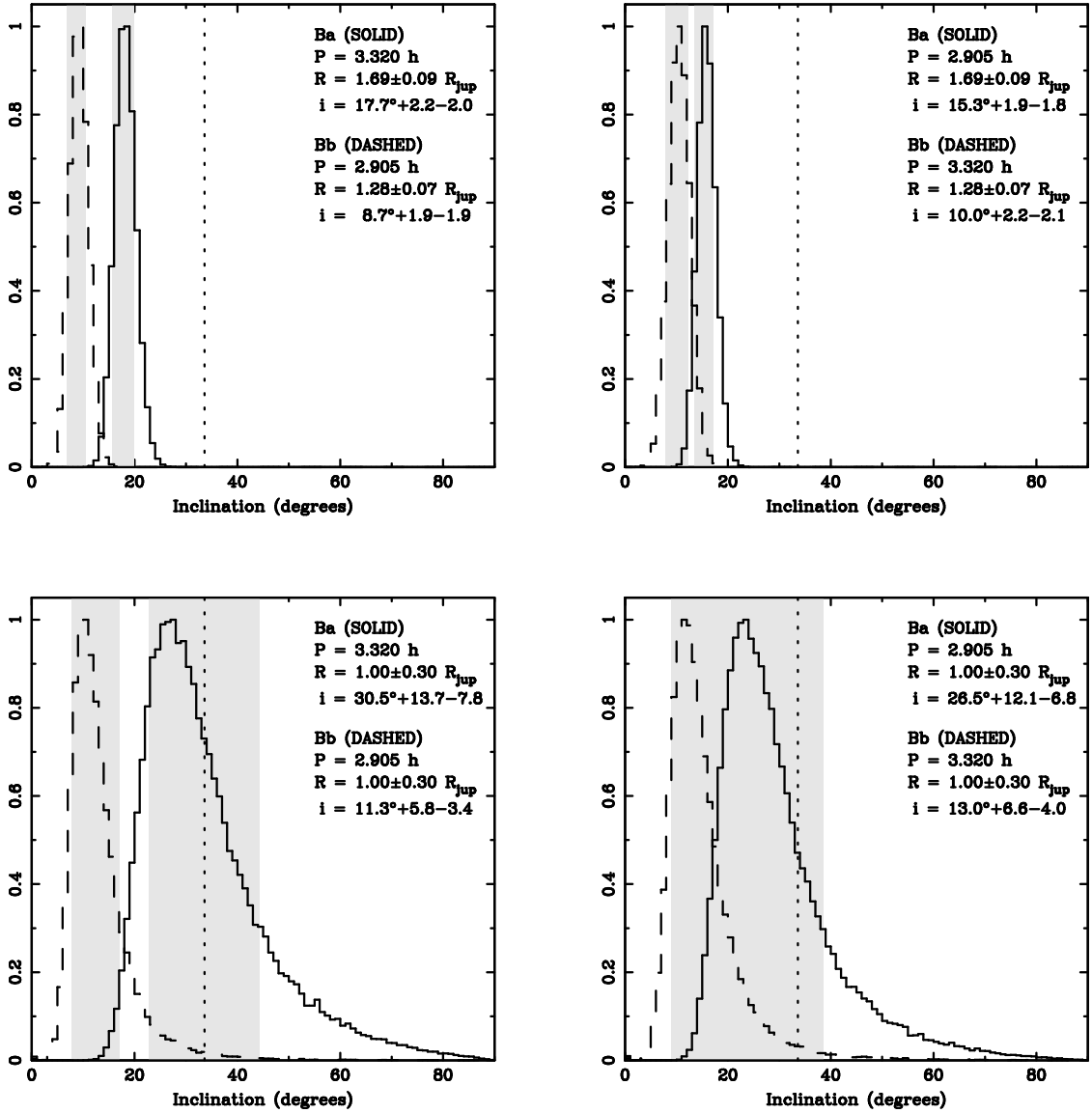


Fig. 6.— Peak normalised distributions of the rotational axis inclinations of Ba and Bb from Monte Carlo simulations. Ba distributions are solid line histograms, Bb are the dashed line histograms. The confidence limits for each distribution are shown as a gray box covering 15.9% to 84.1% cumulative limits. The vertical dashed line is the inclination of the perpendicular of the Ba-Bb orbital plane to our line of sight. The upper two panels are for PHOENIX model parameters, and the lower two panels cover an extended range of generic brown dwarf parameters. Each plot represents different input parameters explained in the text and indicated on the figures.

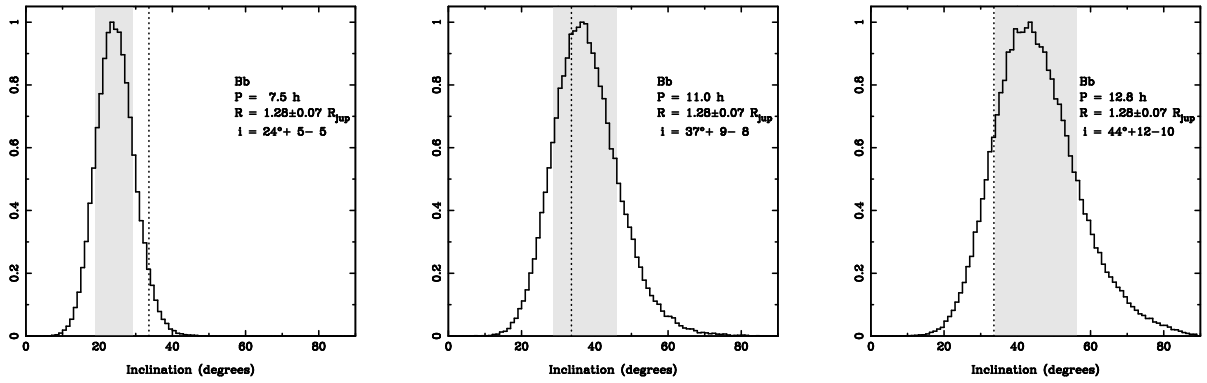


Fig. 7.— Peak normalised distributions of the rotational axis inclinations of Bb from Monte Carlo simulations. The confidence limits for each distribution are shown as a gray box covering 15.9% to 84.1% cumulative limits. The vertical dashed line is the inclination of the perpendicular of the Ba-Bb orbital plane to our line of sight. Each plot represents different input parameters explained in the text and indicated on the figures.